



Bandgap-engineered quaternary $M_xBi_{2-x}Ti_2O_7$ (M : Fe, Mn) semiconductor nanoparticles: Solution combustion synthesis, characterization, and photocatalysis



Gergely F. Samu ^{a,b,c}, Ágnes Veres ^{a,b}, Balázs Endrődi ^{a,b}, Erika Varga ^a, Krishnan Rajeshwar ^{c,*,}, Csaba Janáky ^{a,b,*}

^a Department of Physical Chemistry and Materials Science, University of Szeged, Rerrich Square 1, Szeged H-6720, Hungary

^b MTA-SZTE "Lendület" Photoelectrochemistry Research Group, Rerrich Square 1, Szeged H-6720, Hungary

^c Department of Chemistry and Biochemistry, The University of Texas at Arlington, Arlington, TX 76019, USA

ARTICLE INFO

Article history:

Received 24 November 2016

Received in revised form 24 January 2017

Accepted 10 February 2017

Available online 14 February 2017

Keywords:

Solution combustion synthesis
Bandgap engineering
Dye-degradation
Bismuth titanate
Quaternary metal oxide

ABSTRACT

Ternary and quaternary metal oxides form a rapidly emerging class of new functional materials tackling the grand challenge of efficient solar energy harvesting. Currently the main interest is devoted to the characteristics of these materials and little consideration has been given to their preparation. Solution combustion synthesis (SCS) is considered a green and sustainable alternative to the widely employed energy- and/or time-consuming synthesis methods. In this study, SCS was employed to prepare $Bi_2Ti_2O_7$ and to perform bandgap engineering through foreign ion (Fe, Mn) incorporation. The synthesized materials were characterized by powder X-ray diffraction, transmission electron microscopy, energy-dispersive X-ray microanalysis, diffuse reflectance UV-vis and Raman spectroscopy, and surface area determination via N_2 adsorption. We found that nanocrystalline materials were formed during the SCS synthesis. Further, the phase composition of these materials and the amount of the foreign metal ions incorporated in the parent structure, could be effectively controlled. Consequently, the SCS technique provided a simple and reliable tool for bandgap engineering. The photocatalytic activity of the materials was tested through methyl orange degradation, and the intrinsic photocatalytic activity of the various samples were compared after deconvoluting the effect of their vastly different specific surface areas.

© 2017 Elsevier B.V. All rights reserved.

1. Introduction

Efficient utilization of solar energy is one of the key challenges in solving the imminent energy and environmental challenges facing the world nowadays. Solar energy utilization can be realized through thermal and electrical energy production [1], environmental remediation [2,3], and even fuel production [4,5]. All these fields require advanced materials with immensely different properties (e.g., structural, adsorption, and optoelectronic); however a common denominator is to design them to harness a significant portion of the incoming sunlight. An effective strategy to achieve this goal is bandgap engineering, which can be performed through foreign ion

incorporation (doping or alloying, note the distinction [3,6] based on the incorporated amount) into the parent crystal structure.

Interestingly, the focus in this field has shifted toward the materials aspects and less consideration is given to the preparation methods. Thus metal oxides are generally prepared via energy- (e.g., solid-state or ceramic syntheses) and/or time- (e.g., sol-gel and solvothermal synthesis) consuming methods. This fact weighs heavily on the overall environmental footprint of a given material and also affects the energy payback time of a derived solar harvesting device. In this sense, more efficient synthesis techniques must be discovered and developed. A prominent avenue is solution combustion synthesis (SCS), which originates from the ceramic oxide community [7], and recently has begun to gain foothold in the synthesis of semiconductor nanomaterials [8]. Briefly, the synthesis is based on the highly exothermic reaction between a metal nitrate precursor (oxidizer) and an organic compound (fuel). SCS is a highly customizable synthesis technique [9] where the most important properties (e.g., bandgap [10–12], surface area [13,14], crystal phase composition, and crystallinity [15]) of a given photo-

* Corresponding author at: Department of Physical Chemistry and Materials Science, University of Szeged, Rerrich Square 1, Szeged H-6720, Hungary.

** Corresponding author.

E-mail addresses: rajeshwar@uta.edu (K. Rajeshwar), janaky@chem.u-szeged.hu (C. Janáky).

tocatalyst can be readily tuned. Another important feature of SCS is its ability to form complex (ternary or quaternary) oxides and even metastable phases [8,16]. The synthesis procedure can also be adjusted to achieve doping or even alloying with remnant foreign ions from the employed fuel itself (mostly carbon, nitrogen, and sulfur) or from externally added components (e.g., transition metal ions) [16]. This technique was employed in our research groups in the past few years and led to the realization of several photocatalytically active complex oxide materials [17,18] (for further information about SCS see the Supporting Information).

The modification of monometallic (binary) metal oxide parent structures led to the realization of numerous ternary and quaternary oxides in recent years. Complex oxides can address problems stemming from: (i) incomplete light absorption of the solar spectrum (i.e., wide bandgap, see for example the case of TiO_2 [19]), (ii) inadequate band edge positions to drive certain chemical reactions (e.g., H_2 -evolution on WO_3 [20]) or (iii) insufficient long-term stability (e.g., Cu_2O [21]).

The incorporation of $\text{Bi}(\text{III})$ into simple oxide materials has led to a series of transition metal based ternary oxides (e.g., various titanates, tungstates, niobates, and vanadates). Importantly these materials have the potential to outperform their predecessors in terms of electrical and photocatalytic properties [22]. The underlying principle behind the incorporation of $\text{Bi}(\text{III})$ (as also confirmed by theoretical studies [23,24]) is the ability of its 6s orbital to overlap with the highest d orbital of the respective metal. This phenomenon causes an upward shift in the energy of the valence band, effectively reducing the bandgap of the material. Note that there may also be a conduction band shift in such materials, mainly arising from the contribution of the 6p orbitals of the incorporated $\text{Bi}(\text{III})$ to the O 2p dominated conduction band.

In the case of TiO_2 , the incorporation of $\text{Bi}(\text{III})$ can lead to different bismuth-titanate polymorphs. There are four well-established crystal structures, namely: (i) sillenite ($\text{Bi}_{12}\text{TiO}_{20}$), (ii) Aurivillius-type layered perovskite ($\text{Bi}_4\text{Ti}_3\text{O}_{12}$), (iii) pyrochlore ($\text{Bi}_2\text{Ti}_2\text{O}_7$), and (iv) monoclinic ($\text{Bi}_2\text{Ti}_4\text{O}_{11}$). These materials are mainly studied because of their magnetoelectric properties; however an increasing interest has been devoted to their photocatalytic properties [25]. Among these previously mentioned polymorphs, $\text{Bi}_2\text{Ti}_2\text{O}_7$ is considered the most elusive one, because of its metastable nature. It coexists with the more stable $\text{Bi}_4\text{Ti}_3\text{O}_{12}$ in a wide temperature range [26], making it challenging to achieve phase pure composition. The difficulty to distinguish between these two phases is a major root of controversies surrounding the actual physical properties of $\text{Bi}_2\text{Ti}_2\text{O}_7$ (e.g., dielectric properties [26], optical bandgap dispersion (see also Fig. S1), and temperature stability).

A wealth of synthesis techniques were used to prepare $\text{Bi}_2\text{Ti}_2\text{O}_7$ such as aerosol-assisted vapor deposition [27,28], co-precipitation [29,30], reverse micellar [31], solvo- and hydrothermal [32,33], and modified Pechini synthesis [34] (summarized in Table 1). To achieve phase purity (or even just majority) a recurring strategy is to use excess amount of titanium precursor during synthesis [30,33,34]. This additional Ti, however may result in bismuth deficiency in the obtained material, because of structure stabilization through displacements and vacancy formations in the lattice, which also adds to the complexity of this polymorph [34]. A further interesting structural property was pointed out by recent studies [35,36], where phase-pure single crystalline $\text{Bi}_2\text{Ti}_2\text{O}_7$ was stabilized on Y-stabilized zirconia single crystals. The surface of the as-deposited $\text{Bi}_2\text{Ti}_2\text{O}_7$ terminated preferentially in BiO_x sites, which provided the material with an enhanced CO_2 adsorption capacity [36].

$\text{Bi}_2\text{Ti}_2\text{O}_7$ is an indirect bandgap semiconductor, with an absorption edge located at the cusp of the visible light region [31]. Its visible light photocatalytic activity was studied through photocatalytic dye degradation tests (a summary is given in Table S1) as well as in the photocatalytic evolution of H_2 (using sacrificial

e^- donor) [34]. It was also demonstrated that the charge separation in $\text{Bi}_2\text{Ti}_2\text{O}_7$ is improved through the formation of composites with rGO (reduced graphene oxide) [38,39], TiO_2 nanotubes [40], and $\text{Bi}_4\text{Ti}_3\text{O}_{12}$ [41]. Both theoretical and experimental evidence in the literature suggests that the incorporation of foreign transition metal ions into the $\text{Bi}_2\text{Ti}_2\text{O}_7$ structure can effectively shift its absorption edge toward the visible region. DFT calculations were carried out on both $\text{Bi}(\text{III})$ [42,43] and $\text{Ti}(\text{IV})$ [44] substitutions in the structure, where the former situation was found to be more feasible. This notion was further bolstered by experimental results where the incorporation of $\text{Fe}(\text{III})$ [37,45,46] and $\text{Mn}(\text{II})$ [47] was studied on samples synthesized by a modified reverse micelle method.

The aim of the current study was to use SCS to prepare pyrochlore phase $\text{Bi}_2\text{Ti}_2\text{O}_7$ and study the effect of the synthesis parameters on the phase composition. SCS has been used for the preparation of other bismuth-titanate polymorphs [48,49]; however to the best of our knowledge, there is no precedent study in the literature for this particular phase. We will demonstrate below that careful modification of the SCS protocol (by adding foreign ions of $\text{Fe}(\text{III})$ and $\text{Mn}(\text{II})$ into the precursor solution) can result in bandgap narrowing. The efficacy of SCS is also compared to other, conventional methods. Finally, insights on the photocatalytic performance of these new materials are presented, taking into account all the governing parameters (e.g., surface area, light absorption, crystallinity, and dye adsorption properties).

2. Experimental

2.1. Materials

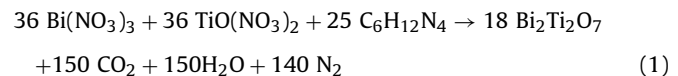
For the preparation of $\text{Bi}_2\text{Ti}_2\text{O}_7$, bismuth nitrate pentahydrate – $\text{Bi}(\text{NO}_3)_3 \cdot 5\text{H}_2\text{O}$ (Alfa Aesar, ACS reagent, 98%) and titanium oxonitrate – $\text{TiO}(\text{NO}_3)_2$ were used as metal precursors, while urea – $\text{CO}(\text{NH}_2)_2$ (Alfa Aesar) and hexamethylenetetramine (HMT) – $\text{C}_6\text{H}_{12}\text{N}_4$ (Sigma Aldrich, ACS grade, 99%) acted as fuels. All the precursors were dissolved in deionized water (DI, Millipore, $18\text{ M}\Omega\text{ cm}$) and nitric acid – HNO_3 (VWR, Analar Normapur[®]).

For the preparation of $\text{TiO}(\text{NO}_3)_2$ precursor titanium isopropoxide – $\text{Ti}(\text{i-OC}_3\text{H}_7)_4$ (Sigma-Aldrich, 97%) was used, which was dissolved in isopropyl alcohol – $\text{C}_3\text{H}_8\text{O}$ (VWR, HiperSolv Chromanorm[®]) as detailed in the Supporting Information.

For the alloying experiments, anhydrous iron(III) chloride – FeCl_3 (VWR, 98%), iron(III) nitrate nonahydrate – $\text{Fe}(\text{NO}_3)_3 \cdot 9\text{H}_2\text{O}$ (Sigma-Aldrich, ACS reagent, 98%), and manganese(II) nitrate tetrahydrate $\text{Mn}(\text{NO}_3)_2 \cdot 4\text{H}_2\text{O}$ (Alfa Aesar, ACS reagent, 98%) were used as the sources of transition metal ions. All materials were of the highest purity commercially available, and were used without further purification.

2.1.1. Synthesis of $\text{Bi}_2\text{Ti}_2\text{O}_7$

Syntheses with different fuel-to-oxidizer (F/O) ratios were investigated. The composition of these mixtures were determined based on propellant chemistry considerations [50]. Briefly, $\text{Bi}(\text{NO}_3)_3 \cdot 5\text{H}_2\text{O}$ and $\text{TiO}(\text{NO}_3)_2$ were both considered as oxidizers and urea or HMT as the fuels. Through the determination of their respective valences, the stoichiometric composition was calculated (only shown for HMT):

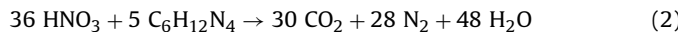


Dissolution of $\text{Bi}(\text{NO}_3)_3 \cdot 5\text{H}_2\text{O}$ requires the addition of HNO_3 to the solution, which can also act as an oxidizer in the reaction (this

Table 1Summary and features of available synthesis methods to prepare $\text{Bi}_2\text{Ti}_2\text{O}_7$. RT stands for room temperature.

Material	Synthesis method			Phase composition	Comments	Ref.
	Description	Duration, temperature	Heat treatment			
$\text{Bi}_2\text{Ti}_2\text{O}_7$ thin films	Sol-gel method	Synthesis at RT (duration not available) followed by film formation at $T=60^\circ\text{C}$ for 1 h	$T=300\text{--}900^\circ\text{C}$ for 30 min	$T < 500^\circ\text{C}$ amorphous, $500^\circ\text{C} < T < 700^\circ\text{C}$ TiO_2 minority phase with $\text{Bi}_2\text{Ti}_2\text{O}_7$ majority phase, $T > 700^\circ\text{C}$ $\text{Bi}_2\text{Ti}_4\text{O}_{11}$	–	[25]
$\text{Bi}_2\text{Ti}_2\text{O}_7$ powder	Co-precipitation method followed by microwave sintering	Synthesis at RT (duration not available)	$T=550^\circ\text{C}$ for 16 h and microwave sintering at $T=1200^\circ\text{C}$	Phase pure $\text{Bi}_2\text{Ti}_2\text{O}_7$	Color change with $\text{Bi}_4\text{Ti}_3\text{O}_{12}$ impurity	[26]
$\text{Bi}_2\text{Ti}_2\text{O}_7$ thin films	Aerosol assisted chemical vapor deposition	1 h, $T=600^\circ\text{C}$	$T=600^\circ\text{C}$ for 12 h	Phase pure $\text{Bi}_2\text{Ti}_2\text{O}_7$	$E_{\text{FB}} = -0.38\text{ V}$ vs. Ag/AgCl in 1.0 M NaOH and a $j_{\text{ph, max}} = 3.0\text{ }\mu\text{A cm}^{-2}$	[27]
$\text{Bi}_2\text{Ti}_2\text{O}_7$ porous microspheres	Aerosol-spray assisted surfactant self-assembly	$T=350^\circ\text{C}$ (duration not available)	$T=600^\circ\text{C}$ for 6 h	$T < 500^\circ\text{C}$ amorphous, $\text{Bi}_4\text{Ti}_3\text{O}_{12}$ minority phase with $\text{Bi}_2\text{Ti}_2\text{O}_7$ majority phase	–	[28]
$\text{Bi}_2\text{Ti}_2\text{O}_7$ powder	Co-precipitation method	Just below RT for 3–4 h	$T=400\text{--}500^\circ\text{C}$ for 16 h	$T < 450^\circ\text{C}$ amorphous, $T < 470^\circ\text{C}$ phase pure $\text{Bi}_2\text{Ti}_2\text{O}_7$, $T > 470^\circ\text{C}$ $\text{Bi}_4\text{Ti}_3\text{O}_{12}$ minority phase with $\text{Bi}_2\text{Ti}_2\text{O}_7$ majority phase	To minimize bismuth loss through volatilization calcination was performed in a Bi_2O_3 containing closed crucible	[29]
$\text{Bi}_2\text{Ti}_2\text{O}_7$ powder	Co-precipitation method	$T=60^\circ\text{C}$ (duration not available)	$T=600^\circ\text{C}$ for 16 h	$\text{Bi}_2\text{Ti}_2\text{O}_7$ majority phase with $\text{Bi}_2\text{Ti}_4\text{O}_{11}$ and TiO_2 minority phases	In the stoichiometric mixture $\text{Bi}_4\text{Ti}_3\text{O}_{12}$ was also present, however the use of excess Ti eliminated this particular phase	[30]
$\text{Bi}_2\text{Ti}_2\text{O}_7$ nanorods	Reverse micelle based method	Synthesis at RT (duration not available)	$T=100^\circ\text{C}$ overnight in N_2 , $T=500\text{--}700^\circ\text{C}$ for 6 h in oxygen atmosphere	Non-calcined sample was amorphous, $650^\circ\text{C} < T < 750^\circ\text{C}$ phase pure $\text{Bi}_2\text{Ti}_2\text{O}_7$, $T > 750^\circ\text{C}$ $\text{Bi}_2\text{Ti}_2\text{O}_7$ majority phase with $\text{Bi}_2\text{Ti}_4\text{O}_{11}$	Nanorod formation at 650°C	[31]
$\text{Bi}_2\text{Ti}_2\text{O}_7$ hollow microspheres	Solvothermal method	$T=110^\circ\text{C}$ for 12 h	$T=400\text{--}550^\circ\text{C}$ for 3 h	$T < 450^\circ\text{C}$ amorphous, $T > 450^\circ\text{C}$ phase pure $\text{Bi}_2\text{Ti}_2\text{O}_7$	Phase purity only with Ti excess ($\text{Bi}/\text{Ti} = 0.4$) otherwise Bi_2O_3 and $\text{Bi}_4\text{Ti}_3\text{O}_{12}$ impurities	[33]
$\text{Bi}_2\text{Ti}_2\text{O}_7$ microspheres	Hydrothermal method	$T=180^\circ\text{C}$ for 24 h	–	Phase pure $\text{Bi}_2\text{Ti}_2\text{O}_7$	The effect of OH^- ions on the synthesis (microsphere size) was investigated	[32]
$\text{Bi}_2\text{Ti}_2\text{O}_7$ powder	Pechini sol-gel route	$T=100^\circ\text{C}$ for 18 h with complete decomposition at temperature of 300°C	$T=500\text{--}800^\circ\text{C}$ for 4 h	Phase purity only with Ti excess ($\text{Bi}/\text{Ti} = 0.7$), $\text{Bi}_4\text{Ti}_3\text{O}_{12}$ with $\text{Bi}/\text{Ti} = 1.3$ and $\text{Bi}_2\text{Ti}_4\text{O}_{11}$ with $\text{Bi}/\text{Ti} = 0.5$	–	[34]
Epitaxial $\text{Bi}_2\text{Ti}_2\text{O}_7$ single crystal	Solution chemistry approach	$T=200^\circ\text{C}$ (duration not available)	$T=600\text{--}900^\circ\text{C}$	Non-calcined sample was amorphous, after calcination phase pure $\text{Bi}_2\text{Ti}_2\text{O}_7$	–	[35,36]
$\text{Fe}_x\text{Bi}_y\text{Ti}_2\text{O}_7$	Solid state synthesis	$T=650^\circ\text{C}$ for 6 h	Subsequent sintering at 950°C for 10 h, 1050°C for 5 h and 1100°C for 5 h	Phase pure iron-bismuth titanates were obtained	–	[37]

fact is often neglected in the literature). Accordingly the reaction below was considered in every case:



A typical reaction mixture was calculated to yield 2.0 g of $\text{Bi}_2\text{Ti}_2\text{O}_7$. For this, 3.2 g of $\text{Bi}(\text{NO}_3)_3 \cdot 5\text{H}_2\text{O}$ was dissolved in 16 cm³ of 2.0 M HNO_3 . This transparent solution was added to the other precursor solution, containing stoichiometric amount of $\text{TiO}(\text{NO}_3)_2$ dissolved in isopropanol. To this mixture, the calculated amount of HMT or urea was added, which was previously dissolved in 10 cm³ of DI water. The amount was appropriate to satisfy the F/O ratio (as corrected for the added HNO_3 amount, according to Eq. (2)). The mixture was preheated on a hotplate for ~30 min at 200 °C to evaporate the 2-propanol and H_2O present in the solution. The obtained gel-like material was then transferred to a muffle furnace preheated to 350 °C regardless of the used fuel (see Fig. S3 for TGA-DSC analysis of the synthesis). As summarized in Table S2, different F/O ratios were employed. At this point, we call attention to the fact that neglecting reaction (2) in the calculation of the required amount of the fuel leads to a notable difference between the actual and the desired F/O ratios. Consider that a F/O ratio of 1.0 without taking into account the added HNO_3 (Eq. (2)) would correspond to an actual F/O ratio of only 0.5.

A smoldering-type combustion was observed in all cases, which lasted for several seconds. When SCS was completed, the obtained material was washed thoroughly with DI water to remove the soluble residues, filtered, and dried in an oven at 100 °C. Thereafter each sample was ground to a fine powder in a mortar and pestle, and annealed at 550 °C for 1 h if indicated.

2.1.2. Synthesis of alloyed $\text{Bi}_2\text{Ti}_2\text{O}_7$ with Fe(III) and Mn(II)

The incorporation of Fe(III) and Mn(II) into $\text{Bi}_2\text{Ti}_2\text{O}_7$ was studied using HMT as fuel. Compounds with composition of $\text{M}_x\text{Bi}_{2-x}\text{Ti}_2\text{O}_7$ were prepared, where $x = 0.01, 0.05, 0.10, 0.25$ and 0.50 M: Fe(III) or Mn(II).

In the case of Fe(III), the effect of anions was also studied by using FeCl_3 or $\text{Fe}(\text{NO}_3)_3$ as the iron source. To calculate the necessary amount of iron precursor, the previously specified reaction (Eq. (1)) was modified so that the desired alloying ratios could be achieved (for more details see Eqs. (S3) and (S4)).

2.2. Physical characterization

UV-vis diffuse reflectance spectra (DRS) were recorded using a PerkinElmer Lambda 35 instrument equipped with an integrating sphere. Raman spectra were obtained with a Thermo Scientific™ DXR™ Raman microscope at an excitation wavelength of 780 nm, applying 10 mW laser power, and averaging 30 spectra with an exposure time of 2 s. The X-ray diffraction (XRD) patterns were recorded on a Siemens D500 X-ray diffractometer with $\text{Cu K}\alpha$ ($\lambda = 0.1542$ nm) as the radiation source at ambient temperature, in the 10–80° (2θ) range applying 0.02° (2θ) step size and 1.0° min⁻¹ scan rate. For Rietveld refinement, the GSAS [51] software was used with an EXPGUI [52] graphical user interface. Transmission electron microscopic (TEM) investigation was performed using a FEI Tecnai™ G² 20 X-Twin type instrument, operating at an acceleration voltage of 200 kV. Energy-dispersive X-ray spectroscopy (EDX) was carried out with a Hitachi S-4700 FE-SEM instrument. For XPS studies, the powder samples were pressed into pellets with ca. 1 cm diameter and a few tenths of μm thickness. The XP spectra were taken with a SPECS instrument equipped with a PHOIBOS 150 MCD 9 hemispherical electron energy analyzer, using $\text{Al K}\alpha$ radiation ($\hbar\nu = 1486.6$ eV). The X-ray gun was operated at 210 W (14 kV, 15 mA). The analyzer was operated in the FAT mode, with the pass energy set to 20 eV. The binding energy scale was corrected by fixing the $\text{Ti } 2\text{p}_{3/2}$ peak to 458.9 eV. Specific surface area

of the photocatalyst samples was determined by a Micromeritics gas sorption analyzer (Quantachrome NOVA 3000) at 77 K in liquid nitrogen. Both the adsorption and desorption branches of the isotherms were determined. Prior to measurements, the samples were pre-treated in vacuum (ca. 0.01 Torr) at 353 K for 12 h. The sample holder was loaded with ca. 0.1–0.3 g sample. The adsorption isotherms were analyzed using the BET-equation. To monitor the mass loss and heat exchange of the combustion reaction thermogravimetric analysis/differential scanning calorimetry (TGA/DSC) was performed in a TA Instruments model Q600 instrument. The precursor mixtures were placed in an alumina crucible in air atmosphere with a gas flow rate of 100 ml min⁻¹ at a heating rate of 10 °C min⁻¹.

2.3. Electrochemical, photoelectrochemical, and photocatalytic measurements

All electrochemical measurements were performed with an Autolab PGSTAT302 potentiostat/galvanostat equipped with an FRA32 M module, in a classical one-compartment, three-electrode electrochemical cell. The powder samples were spray-coated from a 2-propanol suspension (10 mg cm⁻³ concentration) on glassy carbon electrodes with an average loading of 0.5 mg cm⁻², and were used as working electrodes. A large Pt foil counterelectrode and an Ag/AgCl/3 M KCl reference electrode completed the cell setup. Photovoltammetry profiles were recorded in 0.1 M Na_2SO_4 electrolyte, using a slow potential sweep (2 mV s⁻¹) in conjunction with interrupted irradiation (0.1 Hz) on the semiconductor-coated electrodes. The light source was a 300 W Hg-Xe arc lamp (Hamamatsu L8251). The radiation source was placed 3 cm away from the working electrode surface. All measurements were performed at room temperature (20 ± 2 °C).

For the electrochemical impedance spectroscopy (EIS) measurements, a closed electrochemical cell was employed, where 1.0 M Na_2SO_4 solution was used as the electrolyte. The electrolyte was purged with Ar gas for 20 min before each measurement. The powdered samples were spray-coated on a gold electrode with an average loading of 0.5 mg cm⁻² and was subsequently sintered at 300 °C for 1 h. For construction of the Mott–Schottky plots, impedance spectra were recorded at different potential values (with $\Delta E = 0.05$ V interval in the range of $E = 0.2$ –(–)0.3 V), in the 1 Hz to 0.1 MHz frequency range, using a sinusoidal excitation signal (10 mV RMS amplitude).

The photocatalytic activity of the pure $\text{Bi}_2\text{Ti}_2\text{O}_7$ and the alloyed ($\text{M}_x\text{Bi}_{2-x}\text{Ti}_2\text{O}_7$, $\text{M} = \text{Mn}$ or Fe) samples was evaluated by photocatalytic degradation of methyl orange (MO, $\text{C}_{14}\text{H}_{14}\text{N}_3\text{NaO}_3\text{S}$) under UV-vis light irradiation. The photocatalytic reactions were carried out in a double-walled photocatalytic immersion well-reactor at 25 ± 1 °C, with continuous stirring and O_2 bubbling. In a typical photocatalytic test, 0.5 g of the catalyst was added to 250 cm³ aqueous solution of MO with a concentration of 5×10^{-5} M. The suspensions were stirred in the dark for 30 min to establish adsorption equilibrium (Fig. S2). The photocatalytic experiments were carried out for 2 h, using a medium pressure mercury lamp (Fisher, TQ 150, $P = 150$ W) as the radiation source. A pyrex filter was used to cut off high energy UV light (≥ 320 nm). The photon flux of the light source was 2.72×10^{-4} Einstein min⁻¹. For the visible (vis) light ($\lambda \geq 400$ nm) experiments, the cooling water in the reactor was replaced by 1.5 M NaNO_2 solution to cut off UV-light irradiation. Aliquots were taken after prescribed periods of time, filtered through Filter-Bio PVDF syringe filter (0.22 μm pore size) then their UV-vis absorbance was recorded on an Agilent 8453 type spectrophotometer. The photocatalytic activity was evaluated following the change of absorbance at 465 nm vs. irradiation time.

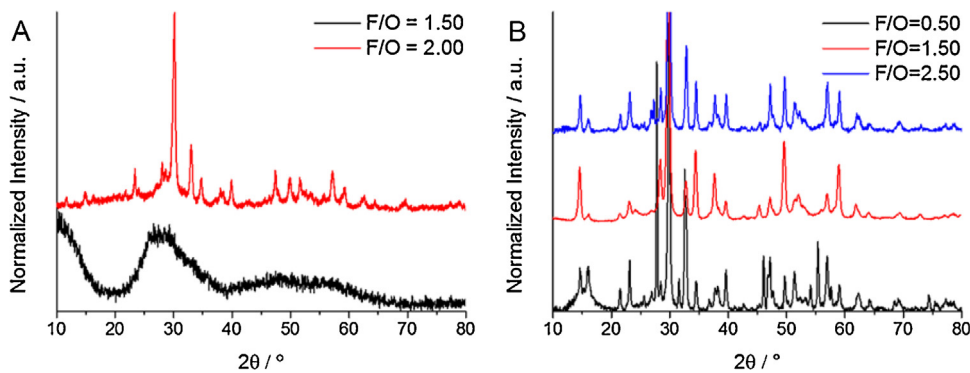


Fig. 1. (A) XRD patterns recorded for the as-is samples prepared with a F/O ratio of 1.5 and 2.0. (B) XRD profiles of the annealed (550 °C) samples prepared with different F/O ratios.

3. Results and discussion

3.1. Preparation of $\text{Bi}_2\text{Ti}_2\text{O}_7$ via SCS

3.1.1. Crystal structure and morphology

XRD analysis was used to characterize the crystallinity of the prepared samples and to reveal the effect of the F/O ratio on phase composition. If not stated otherwise, all results are presented for the case of HMT as fuel. In Fig. 1A the XRD patterns of two as-synthesized samples are presented. The material was completely amorphous at a F/O ratio of 1.5 (and below), but after reaching a F/O ratio of 2.0, crystalline material was obtained. This behavior can be attributed to the relationship between the F/O ratio and flame temperature during the synthesis [14]. As the F/O ratio increases, the heat supplied by the reaction is capable of sustaining higher temperatures, thus producing inherently crystalline materials. The as synthesized F/O = 2.00 sample had a mixed phase composition of Bi_2O_3 (JCPDS 71-2274), $\text{Bi}_2\text{Ti}_2\text{O}_7$ (JCPDS 32-0118), and $\text{Bi}_4\text{Ti}_3\text{O}_{12}$ (JCPDS 35-0795). To completely eliminate any residual amorphous phase, a subsequent annealing step ($t = 1$ h at $T = 550$ °C, air atmosphere) was employed. This temperature was chosen in accordance with the reported thermal stability of the pyrochloric phase (up to 670 °C) [26] and the TGA-DSC data recorded for the precursor mixture, simulating the SCS (Fig. S3). The diffraction patterns in Fig. 1B show that the annealing indeed improved the crystallinity of the samples, but the sample were still multiphasic.

To quantify the phase composition of the obtained materials at different F/O ratios (in the range of 0–2.5), Rietveld refinement was carried out in each case [53]. A typical refinement (for F/O = 1.4) is shown in Fig. 2A, where the measured data, the fitted curve, and the

residual plot are presented. Note that all diffractions are assigned to the respective $\text{Bi}_2\text{Ti}_2\text{O}_7$ (P) or $\text{Bi}_4\text{Ti}_3\text{O}_{12}$ (A) phases. As seen in Fig. 2B the phase composition strongly depends on the employed F/O ratio, and a volcano-type plot was obtained for the $\text{Bi}_2\text{Ti}_2\text{O}_7$ amount in the samples. In addition, the fuel-deficient regime favored the formation of Bi_2O_3 , as a minority phase. Most importantly, phase composition analysis furnished evidence that SCS is a reproducible synthesis technique (see error bars for the samples with the highest $\text{Bi}_2\text{Ti}_2\text{O}_7$ content) and that precise phase composition control can indeed be achieved.

Similar experiments were carried out using urea as the fuel (Fig S4A). The phase composition of the samples exhibited a similar trend (Fig. S4B) to that shown earlier for HMT, so we may conclude that the nature of the fuel does not affect the appearance of the minority phases. After an initial Bi_2O_3 rich region the fraction of $\text{Bi}_2\text{Ti}_2\text{O}_7$ peaked at around F/O = 1.00, followed by a $\text{Bi}_4\text{Ti}_3\text{O}_{12}$ rich region. The difference in the position of the volcano summit for the two fuels was attributed to the different energetics of the fuel-oxidizer reaction. To further underline the importance of SCS (apart from producing inherently crystalline materials) a sample was prepared without any added fuel (denoted as F/O = 0). This material exhibited similar characteristics to samples prepared under fuel-deficient conditions (initially amorphous nature with Bi_2O_3 rich multiphasic nature after annealing, the XRD pattern is shown in Fig. S5). From this point all the presented results were obtained using HMT as the fuel. To gain further insight on the structural features of the samples, Raman spectroscopic measurements were carried out (Fig. S6). The Raman spectra of the materials showed good alignment with the XRD results and their detailed analyses can be found in the Supporting Information.

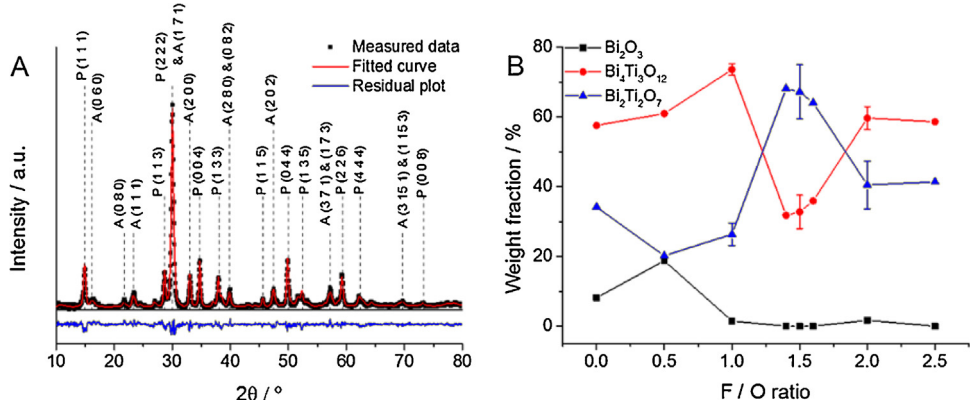


Fig. 2. (A) Rietveld refinement of the XRD pattern recorded for the sample prepared with a F/O ratio of 1.4. P and A stands for $\text{Bi}_2\text{Ti}_2\text{O}_7$ and $\text{Bi}_4\text{Ti}_3\text{O}_{12}$, respectively. (B) The derived phase composition vs. F/O ratio curves (the error bars were determined from measurements on three different sample batches).

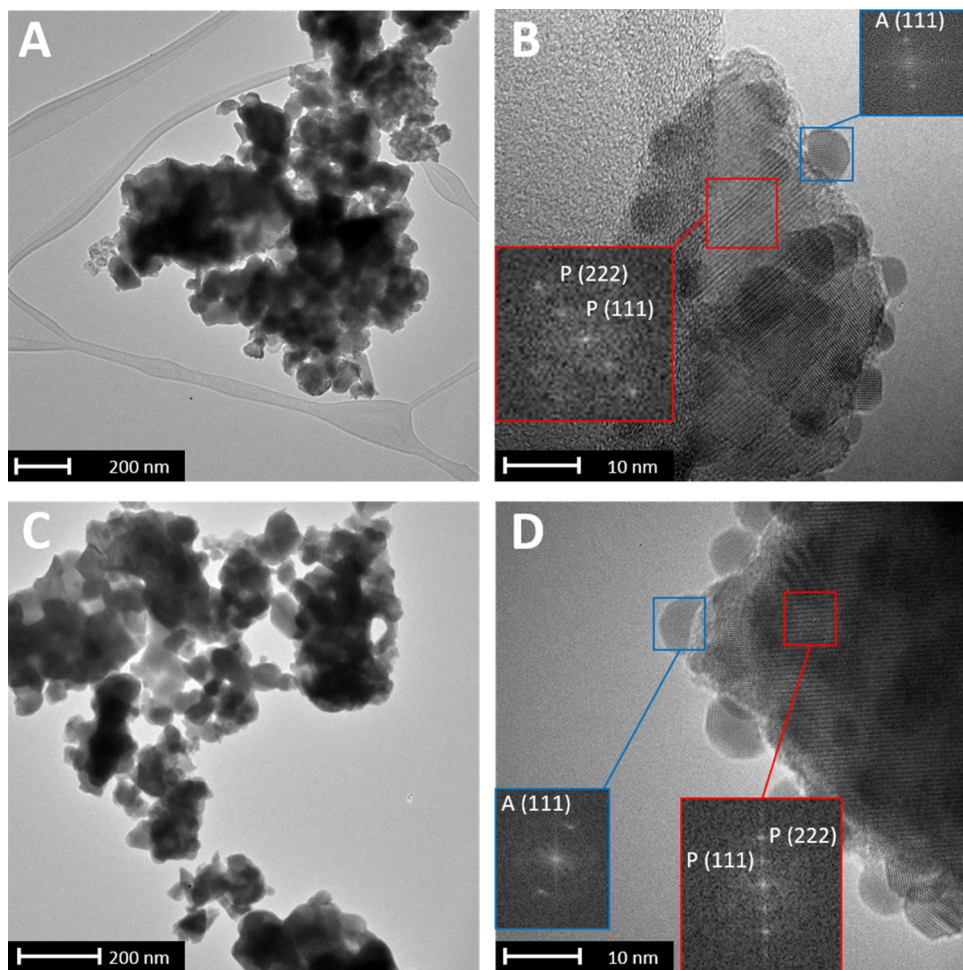


Fig. 3. TEM images of as-synthesized (A and B) and 550 °C annealed (C and D) bismuth titanate samples prepared with a F/O ratio of 2.0. The insets (B and D) show numerical FFT patterns of the highlighted areas (blue – $\text{Bi}_4\text{Ti}_3\text{O}_{12}$ phase, (A: Aurivillius), red – $\text{Bi}_2\text{Ti}_2\text{O}_7$ (P: pyrochlore)). (For interpretation of the references to color in this figure legend, the reader is referred to the web version of the article.)

To investigate the morphology of the samples, TEM images of the F/O = 2.0 samples were recorded before and after thermal anneal (Fig. 3). The as-synthesized material consists of 61 ± 35 nm sized primary particles, fused together because of the highly exothermic synthesis conditions (Fig. 3A and B). This overall morphology was not changed notably during the subsequent heat treatment (Fig. 3C and D). Only a slight increase (~ 10 nm) in the mean particle size was observed, as deduced from the size distribution curves in Fig. S8A. Closer inspection revealed that the agglomerates consist of highly crystalline platelets, decorated with smaller spherical particles, with a mean particle size of 6 ± 1 nm (see also Fig. S8B for size distribution). From HR-TEM images, the lattice spacings were calculated and the platelets were identified as the $\text{Bi}_2\text{Ti}_2\text{O}_7$ phase ($d_{222} = 0.300$ nm) and the spheroids as the $\text{Bi}_4\text{Ti}_3\text{O}_{12}$ phase ($d_{111} = 0.370$ nm). To better analyze the HR-TEM images, Fast Fourier Transform FFT of certain parts of the images were carried out (Fig. 3B and D).

3.1.2. Optical properties

The optical properties of the annealed materials were evaluated by UV-vis DRS. The light absorption properties were highly dependent on the presence of minority phases in the samples (Fig. 4A). $\text{Bi}_2\text{Ti}_2\text{O}_7$ is an indirect bandgap semiconductor [24], thus to determine the bandgap of the materials the Tauc plot was derived by plotting $(\alpha h\nu)^{0.5}$ vs. $h\nu$ (Fig. 4A inset). The intersection of the tangent line with the horizontal axis yielded the bandgap value. The

influence of the F/O ratio on the determined bandgap values is presented in Fig. 4B. These values (between 2.79 and 2.89 eV) are within the range gathered from the literature (Fig. S1), except in the case of F/O = 0.5. In this sample, a conspicuous shoulder around 450–550 nm was observed, which translates to an indirect bandgap value of 2.29 eV (Fig. 4A inset). This was ascribed to the presence of Bi_2O_3 in this sample (as also confirmed by XRD).

3.2. Incorporation of metal ions into the structure: the case of Fe(III)

3.2.1. Structure and composition

Compounds with the composition, $\text{Fe}_x\text{Bi}_{2-x}\text{Ti}_2\text{O}_7$, where $x = 0.01, 0.05, 0.10, 0.25$, and 0.50 were prepared using FeCl_3 and $\text{Fe}(\text{NO}_3)_3$ precursors. The chosen F/O ratio for these experiments was 2.0, because of the incomplete nature of the SCS at lower F/O ratios. In Fig. 5A the XRD patterns of the samples prepared with $\text{Fe}(\text{NO}_3)_3$ are shown. The first important observation was that the increase in the added Fe(III) amount supported formation of the pyrochlore phase (see also the diminishing intensity of the $\text{Bi}_4\text{Ti}_3\text{O}_{12}$ related diffractions, marked with an asterisk in Fig. 5A). Furthermore, a gradual peak shift to higher 2θ values was observed for the pyrochlore related diffractions as the incorporated Fe(III) amount increased (see Fig. 5B for the shift of the (622) reflection at $2\theta \approx 59^\circ$). This positive shift indicated contraction of the $\text{Bi}_2\text{Ti}_2\text{O}_7$ unit cell with increasing Fe(III) incorporation into the lattice (shown

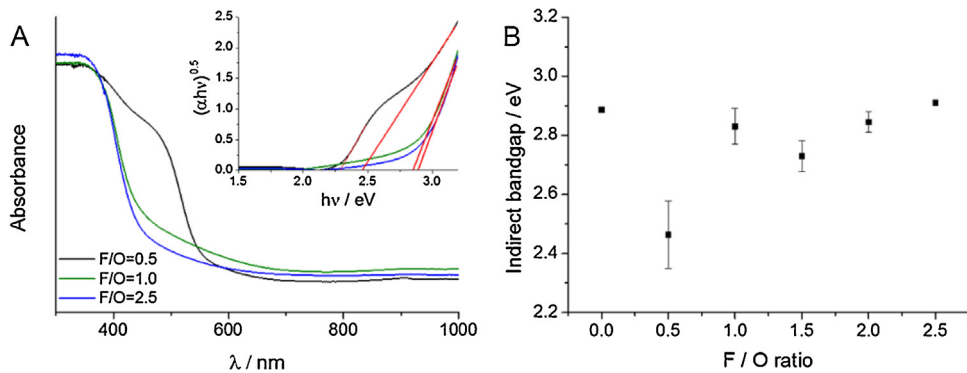


Fig. 4. (A) UV-vis DRS of bismuth titanate samples synthetized with various F/O ratios, where the inset shows the respective Tauc-plots. (B) The effect of the F/O ratio on the bandgap of the prepared materials (the error bars were determined from measurements on three different batches).

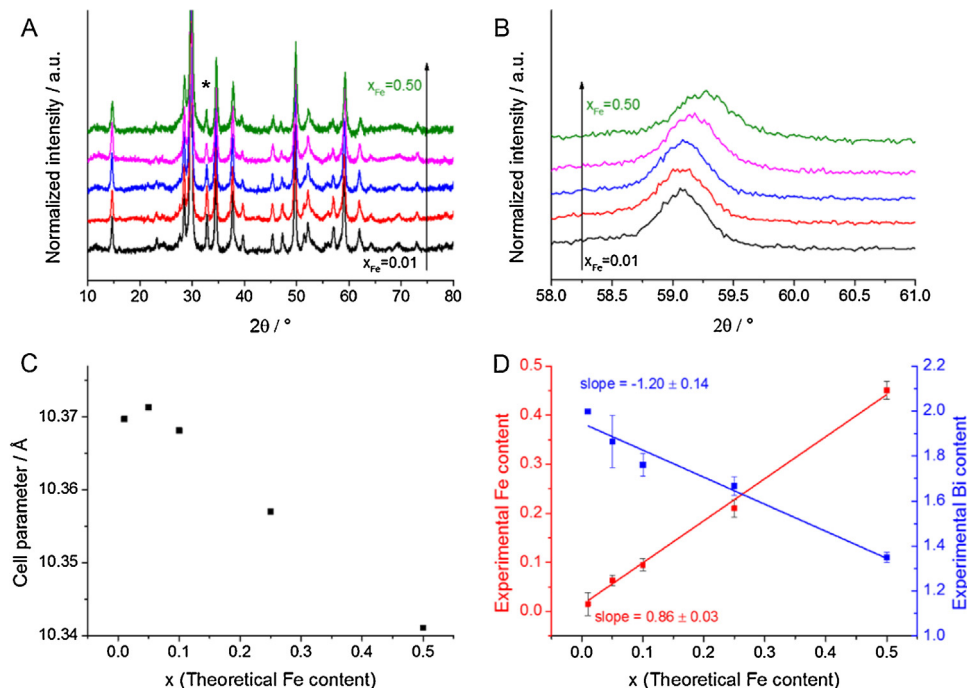


Fig. 5. (A) XRD patterns recorded for the annealed $\text{Fe}_x\text{Bi}_{2-x}\text{Ti}_2\text{O}_7$ samples, where $x = 0.01, 0.05, 0.10, 0.25$, and 0.50 (prepared with a F/O ratio of 2.0). The asterisk denotes the reflection from the $\text{Bi}_4\text{Ti}_3\text{O}_{12}$ impurity. (B) Magnification of the $\text{Fe}_x\text{Bi}_{2-x}\text{Ti}_2\text{O}_7$ related (622) diffraction. (C) The gradual change in the cell parameter, with increasing Fe-content. (D) The change in elemental composition of the compounds, with increasing Fe-ratio, as determined by EDX measurements.

in Fig. 5C). By examining the crystal ionic radii [54] of the composing elements ($r_{\text{Bi}(\text{III})} = 117 \text{ pm}$, $r_{\text{Fe}(\text{III})} = 69 \text{ pm}$ (low spin) or 79 pm (high spin), and $r_{\text{Ti}(\text{IV})} = 75 \text{ pm}$), Fe(III) incorporation is clearly seen to proceed into crystallographic sites previously occupied by Bi(III) in $\text{Bi}_2\text{Ti}_2\text{O}_7$. In a recent study, a similar unit cell contraction was observed for pure $\text{Bi}_2\text{Ti}_2\text{O}_7$; however in this case it was induced by variation of the precursor composition during the synthesis [34]. In the case of Bi(III) deficient conditions, Ti(IV) incorporation took place into the Bi(III) vacancies [34]. This is in good accordance with our results, as Fe(III) and Ti(IV) have similar crystal ionic radii, thus shrinkage of the unit cell might occur in a similar fashion.

EDX measurements were carried out to determine the amount of Fe(III) incorporated into the crystal lattice (Fig. 5D). With increasing Fe(III) precursor concentration during SCS, a higher amount of iron was incorporated into the compound. Simultaneously, the bismuth content decreased, further validating the proposed Bi(III)–Fe(III) exchange. The slope of both curves approached unity, indicating good agreement between the presumed and actual compositions.

To gain further insights on the chemical state of the incorporated iron, XPS measurements were carried out on the annealed $\text{Fe}_{0.50}\text{Bi}_{1.50}\text{Ti}_2\text{O}_7$ sample. The Fe 2p spectrum (Fig. 6A), possesses characteristic features of Fe(III) present in the compound. The position of the $2p_{3/2}$ line at 711.9 eV is in good agreement with values reported in the literature for Fe(III) containing oxide species [55] (e.g., Fe_2O_3 and FeOOH). Furthermore the 8.1 eV separation of this line and its satellite feature located at 720 eV is also similar to other Fe(III) containing oxides [56]. In the Bi 4f region only two symmetric peaks were observed corresponding to the $4f_{7/2}$ (159.8 eV) and $4f_{5/2}$ (165.1 eV) components with a $\Delta E = 5.3 \text{ eV}$ peak separation. There were no additional features at lower binding energies which confirmed that only Bi(III) is present in the material [35]. In the Ti 2p region, apart from the two Ti 2p levels ($2p_{3/2}$ at 458.9 eV and $2p_{1/2}$ at 464.6 eV), a strong contribution was observed from the $4d_{3/2}$ component of bismuth. The peak shapes were fitted with symmetric Voigt functions and no additional lower binding energy features were necessary to obtain adequate fitting, which confirmed the exclusive presence of Ti(IV) [35]. On the O 1s spectra (not shown

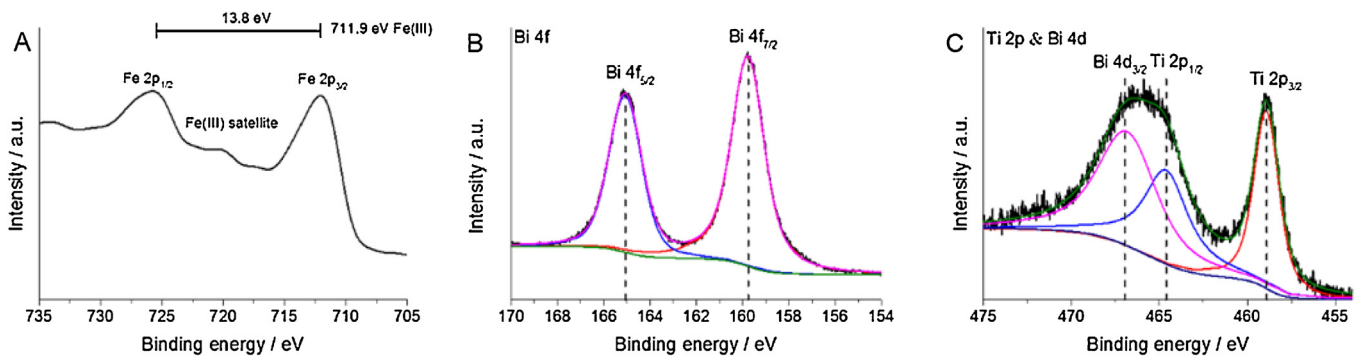


Fig. 6. XP spectra of an annealed $\text{Fe}_{0.50}\text{Bi}_{1.50}\text{Ti}_2\text{O}_7$ sample prepared with a F/O ratio of 2.0, in the (A) Fe 2p region, (B) Bi 4f region and (C) Ti 2p region.

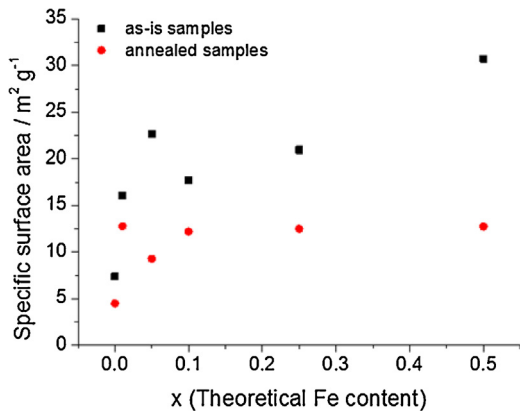


Fig. 7. Composition dependence of the specific surface area, of the various $\text{Fe}_{x}\text{Bi}_{2-x}\text{Ti}_2\text{O}_7$ samples, as derived from BET measurements ($T=77\text{ K}$ in liquid nitrogen).

here) apart from the 531.5 eV main line two other components with higher binding energies could be distinguished. This can be related to either formation of oxygen vacancies [35,57,58] or the presence of surface OH groups. Judging from the single oxidation state of each metal in the compound and the near stoichiometric composition (Fig. 5D), however, the formation of such oxygen vacancies is unlikely. The C 1s spectrum was also recorded, and no evidence of M–C bonding was detected, which indicated that no significant carbon doping/alloying occurred.

Specific surface areas of the samples were measured by N_2 adsorption and analyzed using the BET-isootherm (Fig. 7). The specific surface areas of the samples increased for both the as-is and annealed samples as the Fe content increased. This effect can be attributed to the change in the energetics of the SCS. As discerned from TEM images the particle size distribution curves maxima shifted to smaller values (from 71 nm ($\text{Bi}_2\text{Ti}_2\text{O}_7$) to 63 nm ($\text{Fe}_{0.10}\text{Bi}_{1.90}\text{Ti}_2\text{O}_7$) and 57 nm ($\text{Fe}_{0.50}\text{Bi}_{1.50}\text{Ti}_2\text{O}_7$)). Furthermore, the absence of larger primary particles in the case of the alloyed samples also contribute to the experienced surface area increase (Fig. S9A and B). Notably, the obtained values for the as-is samples were always greater than that of the annealed samples. These values, however, were still below those measured for the benchmark, Aerioxide P25 TiO_2 ($A_{\text{surf.}}=56\text{ m}^2\text{ g}^{-1}$).

3.2.2. Optical properties

UV-vis DRS showed a gradual red shift in the absorption edge as the iron content increased (Fig. 8A). To accurately determine the bandgap of the alloyed compounds, Tauc plots were derived (Fig. S14A). It was found that the bandgap of the compounds was highly composition dependent (Fig. 8B). This trend is well-supported by theoretical predictions, which suggest that the incorporation of Fe(III) into the structure results in a decrease of the bandgap. This

can proceed without the inclusion of mid-gap states into the band structure of $\text{Bi}_2\text{Ti}_2\text{O}_7$ [42,43]. In this manner, a maximum bandgap reduction of 0.7 eV was achieved through successive iron incorporation into the lattice (this is also visible in the color of the samples, see inset of Fig. 8B).

3.2.3. Photoelectrochemical properties

To better understand the exact effect of Fe(III) incorporation on the band structure of the materials photoelectrochemical measurements were carried out. Linear sweep photovoltaic profiles (raw data can be found in Supplementary Information, see Fig. S10A) of the samples were recorded in 0.1 M Na_2SO_3 under periodically interrupted illumination. The negative shift of the open circuit potential under illumination indicated the n-type semiconductor behavior of the materials. The flat-band potential, which is related to the conduction band edge of n-type semiconductors [59,60] can be estimated from the onset potential of photocurrent flow (see Fig. S10A). Mott–Schottky plots were derived from the EIS data (Fig. S10B) to determine the flat-band potential of the materials. An n-type behavior (positive slope in Fig. S10B) was seen for the pristine and $x=0.5$ Fe containing samples (note that these were also the best performing samples in terms of the magnitude of the photocurrent (Fig. S10A)). For the intermediate alloying levels, the charge carrier concentration (i.e., the slope of the Mott–Schottky plot) was very small, which hindered quantification, although the n-type nature was confirmed even in these cases. Similar shift in the conduction band edge could be determined from both the photocurrent onset and the Mott–Schottky plots upon Fe-alloying.

The band diagrams constructed from these data and the determined optical bandgaps are shown in Fig. 9. The band edge positions for TiO_2 and $\text{Bi}_2\text{Ti}_2\text{O}_7$ are in good agreement with previously reported experimental data [61,62]. The incorporation of Fe(III) in the structure of $\text{Bi}_2\text{Ti}_2\text{O}_7$ induced a shift in both the valence and conduction band edge of the material, resulting in a net reduction of the bandgap (Fig. 9). Finally, note that only small photocurrents (typically in the range of several $\mu\text{A cm}^{-2}$) were observed in all the cases (Fig. S10A). This indicates excessive charge carrier recombination (caused by e.g., trap states, low conductivity of the material) and low charge carrier concentration (also confirmed by the Mott–Schottky analysis) which in turn influence the photocatalytic performance of the materials as demonstrated later.

To illustrate the importance of the counter anions employed during SCS, similar syntheses were carried out with FeCl_3 precursor (instead of $\text{Fe}(\text{NO}_3)_3$). The detailed experiments are considered in the Supporting Information (Fig. S11), but briefly it was found that in these cases a BiOCl impurity phase was formed at higher FeCl_3 concentrations ($x=0.25$ and 0.50). The appearance of this minority phase affected both the optical properties and specific surface areas of the samples. In the case of $\text{Fe}_{0.50}\text{Bi}_{1.50}\text{Ti}_2\text{O}_7$ this manifested in a massive surface area increase ($30\text{--}50\text{ m}^2\text{ g}^{-1}$) when

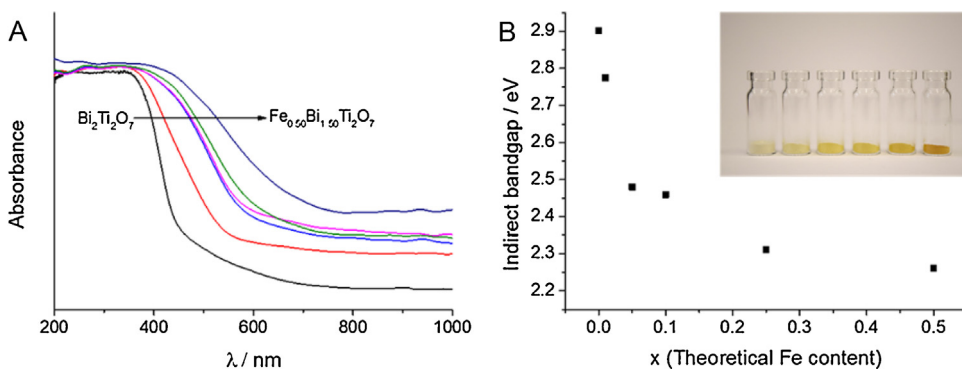


Fig. 8. (A) UV-vis absorbance spectra (derived from the DRS) of the Fe(III)-alloyed $\text{Bi}_2\text{Ti}_2\text{O}_7$ samples. (B) The composition dependence of the indirect bandgap; the inset shows the gradual color change of the compounds.

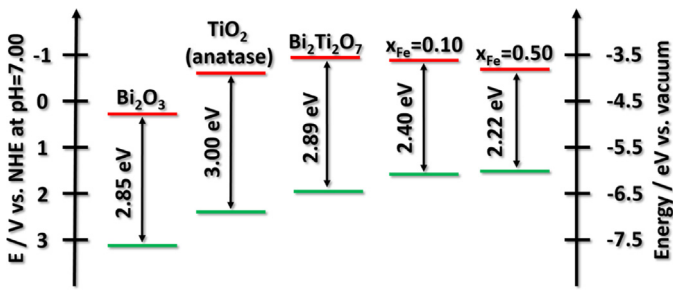


Fig. 9. Band diagrams of Fe(III)-alloyed $\text{Bi}_2\text{Ti}_2\text{O}_7$ and related materials constructed from photoelectrochemical and optical measurements.

BiOCl was present. Furthermore, methyl-orange adsorption measurements revealed strong, specific adsorption of the dye on the surface of the BiOCl impurity phase.

3.3. Incorporation of metal ions into the structure—the case of $\text{Mn}(\text{II})$ ions

3.3.1. Structure and composition

The substitution of $\text{Fe}(\text{NO}_3)_3$ for $\text{Mn}(\text{NO}_3)_2$ in the precursor mixture yielded Mn(III)-alloyed bismuth titanates (as later shown by XPS). As deduced from the recorded XRD patterns (Fig. 10A), a similar behavior was observed as in the case of Fe(III). This includes a notable reduction in the diffraction intensity of the Aurivillius $\text{Bi}_4\text{Ti}_3\text{O}_{12}$ phase and a peak shift of the $\text{Bi}_2\text{Ti}_2\text{O}_7$ related diffractions. Note that both elements have similar crystal ionic radii ($r_{\text{Mn}(\text{III})} = 72$ pm (low spin) or 79 pm (high spin)). EDX measurements indicated a good correlation of the actual composition with the theoretical one (Fig. 10D).

To determine the oxidation state of the incorporated Mn, Mn 2p XP spectra were recorded for the annealed $\text{Mn}_{0.50}\text{Bi}_{1.50}\text{Ti}_2\text{O}_7$ sample (Fig. 11A). Judging from the missing satellite peak related to Mn(II) and the symmetric feature of the main core line at 642.7 eV, the presence of Mn(III) was further established in our sample [63]. Note that usually peak splitting of the Mn 3s XPS signal is used to differentiate between the oxidation states of Mn [63]. In our case, however the interference with the bismuth peaks makes it impossible to evaluate the 3s peaks of Mn. Although in recent studies on Mn-alloyed $\text{Bi}_2\text{Ti}_2\text{O}_7$ the presence of oxygen vacancies was demonstrated [57,58], XP spectra for Bi 4f (Fig. 11B) and Ti 2p (Fig. 11C) showed the presence of single oxidation state for each metal (similarly to the Fe(III)-alloyed samples) in our case.

The specific surface area of the samples were also measured by N_2 adsorption and analyzed by using the BET-isotherm. A similar composition dependence was observed as in the case of Fe(III) incorporation and a summary is given in Fig. S12. This behavior can

also be attributed to the decrease in the particle size (as seen in Fig. S9C and D).

3.3.2. Optical properties

The most prominent features of the absorption spectra was a red shift in the absorption edge and a pronounced increase in the overall, non-characteristic absorption of the materials with the increasing manganese content (Fig. 12A). This increase can be rationalized by the presence of mid-gap states in the electronic structure of the materials as predicted by DFT calculations [42]. The 3d orbitals of the incorporated Mn(III) have a contribution to the valence band of the material and also form both occupied and unoccupied mid band energy states. By employing the Tauc conversion (Fig. S13B) it was found that increasing manganese content in the samples translated to ~ 0.9 eV bandgap reduction (Fig. 12B). We note here that the determined bandgap values carries higher uncertainty for the two highest Mn content, because of the increased non-characteristic absorption in these instances (see also Fig. S13B).

4. Photocatalysis experiments – MO degradation

To probe the photoactivity of the synthesized materials, dye-degradation experiments were carried out, using methyl orange (MO) as a probe. This dye is a popular choice for photodegradation experiments, because most of the discharged pigments by the textile industry have similar structural features (azo compounds) [64]. UV-vis photocatalytic experiments are shown for the unmodified as-is $\text{Bi}_2\text{Ti}_2\text{O}_7$ sample synthesized with a F/O ratio of 2.0 (Fig. 13). A gradual decrease of MO light absorption was observed as the reaction time proceeded, without the formation of any side-products exhibiting UV-vis absorption (Fig. 13A). From the absorption maximum located at 465 nm, the kinetics of the dye degradation was also studied (Fig. 13B). Under visible light irradiation, pristine $\text{Bi}_2\text{Ti}_2\text{O}_7$ outperformed the benchmark P25 photocatalyst (Fig. 13C). This can be rationalized by the extended visible light absorption capability of $\text{Bi}_2\text{Ti}_2\text{O}_7$.

To quantitatively compare the efficiency of the photocatalysts, the apparent reaction rates (k_0) were determined from the equation:

$$-\ln \left(\frac{c}{c_0} \right) = k_0 t \quad (5)$$

where c is the concentration of MO, c_0 is the initial concentration of MO and t is irradiation time. This approach was feasible because the reaction followed pseudo-first order kinetics. The apparent reaction rate (k_0) values were normalized by the BET surface area values to allow meaningful comparison of the specific photocatalytic activity of the catalysts. The obtained values are summarized

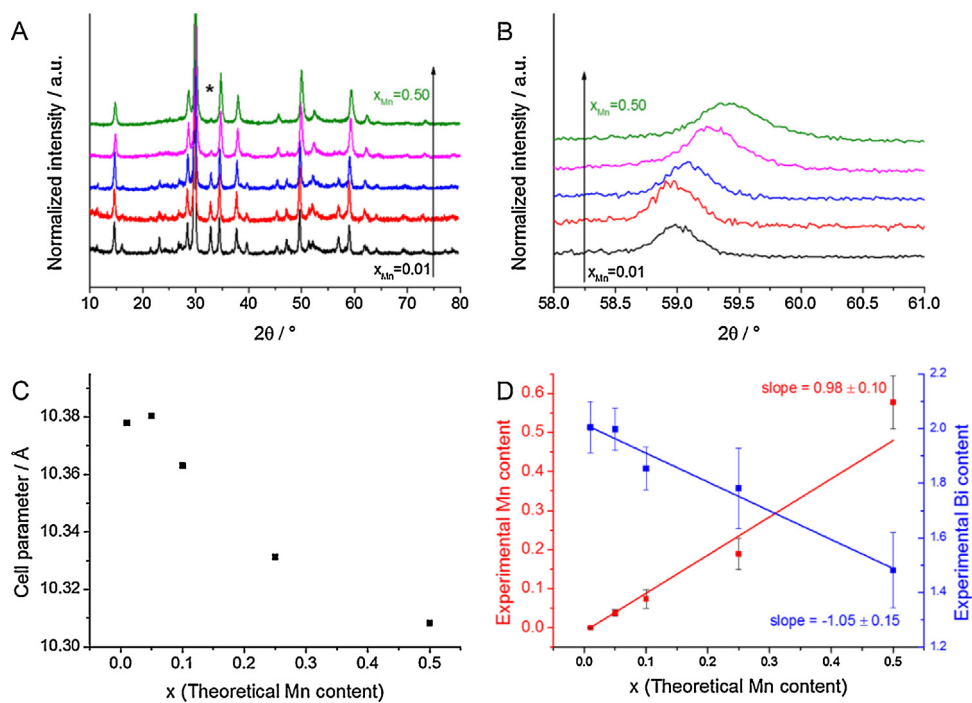


Fig. 10. (A) XRD patterns recorded for the annealed $Mn_xBi_{2-x}Ti_2O_7$ samples, where $x=0.01, 0.05, 0.10, 0.25$, and 0.50 (prepared with a F/O ratio of 2.0). The asterisk denotes the reflection from the $Bi_4Ti_3O_{12}$ impurity. (B) Magnification of the $Mn_xBi_{2-x}Ti_2O_7$ related (622) diffraction. (C) The gradual change in the cell parameter with increasing Mn-content. (D) The change in elemental composition of the compounds with increasing Mn-ratio, as determined by EDX measurements.

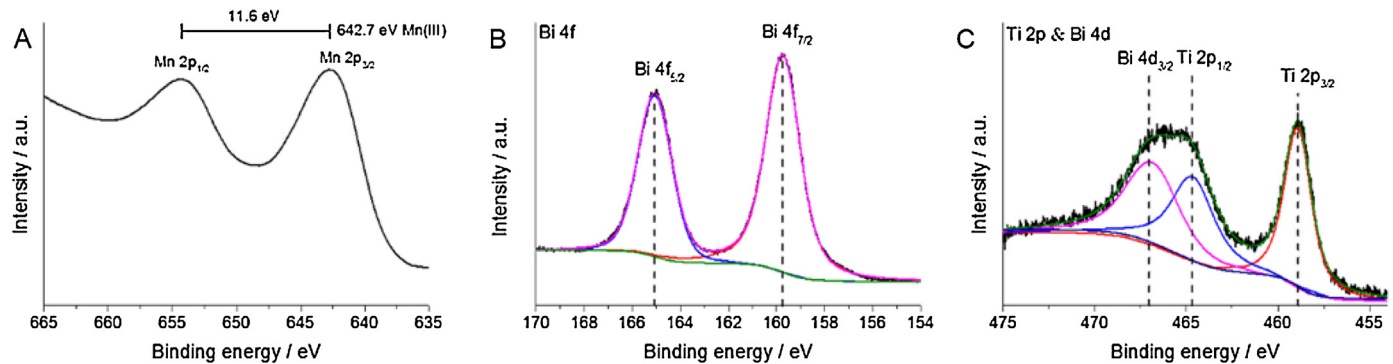


Fig. 11. XP spectra of an annealed $Mn_{0.50}Bi_{1.50}Ti_2O_7$ sample prepared with a F/O ratio of 2.0 in the (A) Mn 2p region, (B) Bi 4f region and (C) Ti 2p region.

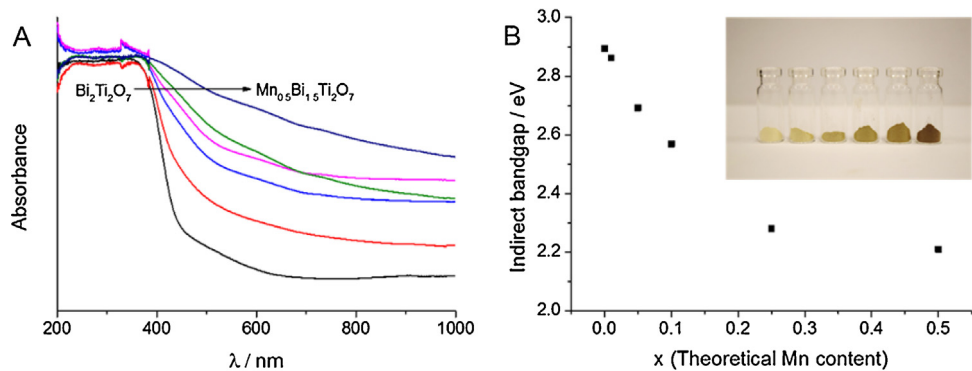


Fig. 12. (A) DRS-derived UV-vis absorbance spectra of the Mn(III)-alloyed $Bi_2Ti_2O_7$ samples. (B) The composition dependence of the indirect bandgap; the inset shows the progressive color change of the compounds.

in Table 2 where the photocatalytic activity of the respective annealed samples are included as well. The higher values obtained for the annealed samples indicated that increased crystallinity after

thermal anneal, improved their photocatalytic activity. Because of the visible light absorption capability of $Bi_2Ti_2O_7$, dye degradation experiments were also carried out by excluding the UV

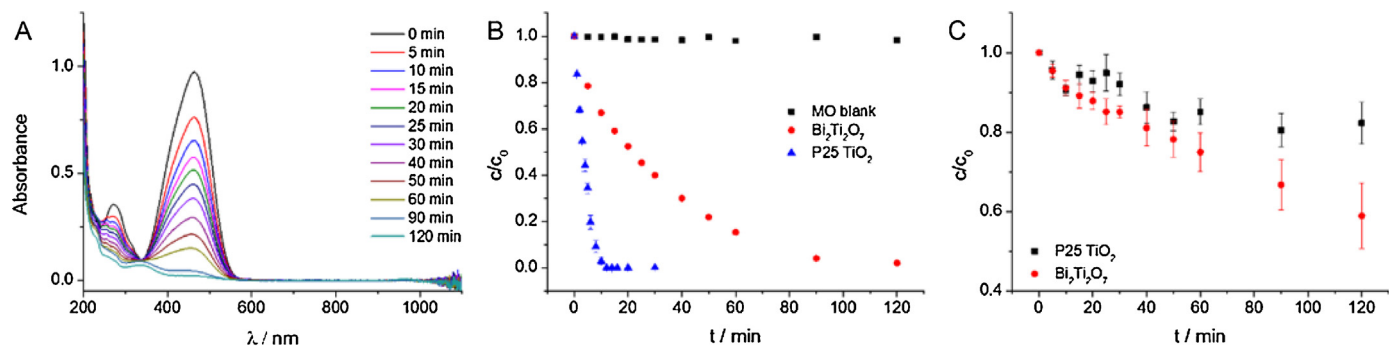


Fig. 13. (A) UV-vis spectra of MO degradation with as-is $\text{Bi}_2\text{Ti}_2\text{O}_7$ prepared with a F/O ratio of 2 with UV-vis irradiation. (B) The derived kinetic curves from the recorded spectra with UV-vis irradiation. (C) The derived kinetic curves for MO degradation with only visible light irradiation for the annealed bismuth titanate sample.

Table 2

Summary of the UV-vis photocatalytic activity of unmodified $\text{Bi}_2\text{Ti}_2\text{O}_7$ prepared with F/O ratio of 2.0.

Sample name	Type of illumination	k'_{norm} ($\text{min}^{-1} \text{m}^{-2}$)
As-is $\text{Bi}_2\text{Ti}_2\text{O}_7$	UV-vis	9.0×10^{-3}
Annealed $\text{Bi}_2\text{Ti}_2\text{O}_7$	UV-vis	1.6×10^{-2}
Aeroxide P25 TiO_2	UV-vis	3.7×10^{-2}
Annealed $\text{Bi}_2\text{Ti}_2\text{O}_7$	Only visible	3.1×10^{-3}
Aeroxide P25 TiO_2	Only visible	6.4×10^{-4}

portion of the irradiation (Fig. 13C). Compared to P25 TiO_2 , superior performance was achieved. The apparent rate constant for MO degradation with $\text{Bi}_2\text{Ti}_2\text{O}_7$ was found to be 5 times higher than what was determined for P25 TiO_2 .

Similar photocatalytic experiments were carried out for the alloyed samples. Interestingly, despite their higher surface area and superior light absorption properties, they performed poorly in dye-degradation experiments. In Fig. S14 the obtained k'_{norm} values for the Fe(III)-alloyed samples are summarized. Rapid deterioration of the photocatalytic activity was observed even at small alloying amounts, similarly to the Mn-alloyed samples. These observations are in accordance to earlier literature precedence, where the incorporation of over 1% of Fe and Mn into the $\text{Bi}_2\text{Ti}_2\text{O}_7$ structure substantially decreased the photocatalytic performance [45–47]. This effect cannot be fully explained by the inclusion of mid-gap states acting as trap states, because the Fe(III)-alloyed samples are presumably free from such motifs [42]. The most plausible explanation for the inferior performance of the alloyed photocatalysts lies in their electronic properties (which is also apparent from their photoelectrochemical properties (Fig. S10A)).

This further draws attention toward the intricate nature of photocatalysis and that the photoactivity of a given material is determined by several different factors [3]. Apart from tuning the optical and structural/morphological properties, it is necessary to also tailor the electronic and surface properties of the catalysts to achieve superior performance. Finally, we note that the deterioration of the photocatalytic performance of the alloyed samples coincides with the disappearance of the impurity $\text{Bi}_4\text{Ti}_3\text{O}_{12}$ phase. Because of the proper alignment of the band positions of these two phases [41]. This in turn can enhance charge separation and can be considered as one of the governing factors in the observed photoelectrochemical and photocatalytic activity of the materials.

5. Summary

In this study, the synthesis of $\text{Bi}_2\text{Ti}_2\text{O}_7/\text{Bi}_4\text{Ti}_3\text{O}_{12}$ was achieved via solution combustion synthesis. The effect of F/O ratio on the phase composition and optical properties was explored. We successfully extended the synthesis technique to prepare quaternary

$\text{Bi}_{2-x}\text{M}_x\text{Ti}_2\text{O}_7$ (M: Fe, Mn) materials as well. The inclusion of foreign metals into the pyrochloric $\text{Bi}_2\text{Ti}_2\text{O}_7$ structure was demonstrated through contraction of the unit cell and alteration of elemental composition. In addition, alloying resulted in the gradual decrease of the bandgap of the compounds. The photocatalytic activity of the samples was evaluated through dye-degradation experiments and compared to a benchmark, Aeroxide P25 TiO_2 . It was found that pure $\text{Bi}_2\text{Ti}_2\text{O}_7$ outperformed the benchmark when only visible irradiation was applied. Despite the extended light absorption properties and superior surface area of the metal-alloyed samples, their photocatalytic performance remained low. Clearly, further electronic property optimization would play a key role in determining the ultimate photocatalytic performance of these materials. The key message of this study is that SCS can be easily extended to the synthesis of complex oxide semiconductor materials. This energy- and time-efficient synthesis technique allows for fast screening of potential photocatalysts. The findings from this study should encourage other researchers to use this technique and thus expand the library of photocatalytically active complex oxide material candidates.

Acknowledgements

The authors thank Dr. János Kiss (Department of Physical Chemistry and Materials Science, University of Szeged) for valuable discussions on the XPS results. CJ gratefully acknowledges the support from the Hungarian Academy of Sciences, through its “Momentum” Excellence Program. GFS gratefully acknowledges support from the Hungarian Initiatives Foundation and the NTP-NFTÖ-16 grant. This research was supported by the “Széchenyi 2020” program in the framework of GINOP-2.3.2-15-2016-00013 “Intelligent materials based on functional surfaces – from syntheses to applications”. KR thanks the National Science Foundation (CHE-1303803) for partial funding support. The authors thank the three anonymous reviewers for their constructive criticisms of an earlier version of this manuscript.

Appendix A. Supplementary data

Supplementary data associated with this article can be found, in the online version, at <http://dx.doi.org/10.1016/j.apcatb.2017.02.036>.

References

- [1] S. Rühle, A.Y. Anderson, H.N. Barad, B. Kupfer, Y. Bouhadana, E. Rosh-Hodesh, A. Zaban, All-oxide photovoltaics, *J. Phys. Chem. Lett.* 3 (2012) 3755–3764.
- [2] K. Rajeshwar, Solar energy conversion and environmental remediation using inorganic semiconductor–liquid interfaces: the road traveled and the way forward, *J. Phys. Chem. Lett.* 2 (2011) 1301–1309.

[3] K. Rajeshwar, A. Thomas, C. Janáky, Photocatalytic activity of inorganic semiconductor surfaces: myths, hype, and reality, *J. Phys. Chem. Lett.* 6 (2015) 139–147.

[4] M.G. Walter, E.L. Warren, J.R. McKone, S.W. Boettcher, Q. Mi, E.A. Santori, N.S. Lewis, Solar water splitting cells, *Chem. Rev.* 110 (2010) 6446–6473.

[5] P.D. Tran, L.H. Wong, J. Barber, J.S.C. Loo, Recent advances in hybrid photocatalysts for solar fuel production, *Energy Environ. Sci.* 5 (2012) 5902–5918.

[6] T.M. Breatnach, B.M. Bartlett, Lowering the band gap of anatase-structured TiO_2 by co alloying with Nb and N: electronic structure and photocatalytic degradation of methylene blue dye, *J. Phys. Chem. C* 116 (2012) 5986–5994.

[7] A.G. Merzhanov, The chemistry of self-propagating high-temperature synthesis, *J. Mater. Chem.* 14 (2004) 1779–1786.

[8] K. Rajeshwar, N.R. de Tacconi, Solution combustion synthesis of oxide semiconductors for solar energy conversion and environmental remediation, *Chem. Soc. Rev.* 38 (2009) 1984–1998.

[9] S.L. González-Cortés, F.E. Imbert, Fundamentals, properties and applications of solid catalysts prepared by solution combustion synthesis (SCS), *Appl. Catal. A Gen.* 452 (2013) 117–131.

[10] Y. Ni, Y. Zhu, X. Ma, A simple solution combustion route for the preparation of metal-doped TiO_2 nanoparticles and their photocatalytic degradation properties, *Dalton Trans.* 40 (2011) 3689–3694.

[11] W. Morales, M. Cason, O. Aina, N.R. de Tacconi, K. Rajeshwar, Combustion synthesis and characterization of nanocrystalline WO_3 , *J. Am. Chem. Soc.* 130 (2008) 6318–6319.

[12] K. Nagaveni, M.S. Hegde, N. Ravishankar, G.N. Subbanna, G. Madras, Synthesis and structure of nanocrystalline TiO_2 with lower band gap showing high photocatalytic activity, *Langmuir* 20 (2004) 2900–2907.

[13] K. Deshpande, A. Mukasyan, A. Varma, Direct synthesis of iron oxide nanopowders by the combustion approach: reaction mechanism and properties, *Chem. Mater.* 16 (2004) 4896–4904.

[14] A.S. Mukasyan, P. Epstein, P. Dinka, Solution combustion synthesis of nanomaterials, *Proc. Combust. Inst.* 31 (2007) 1789–1795.

[15] X. Ma, L. Xue, X. Li, M. Yang, Y. Yan, Controlling the crystalline phase of TiO_2 powders obtained by the solution combustion method and their photocatalysis activity, *Ceram. Int.* 41 (2015) 11927–11935.

[16] F. Li, J. Ran, M. Jaroniec, S.Z. Qiao, Solution combustion synthesis of metal oxide nanomaterials for energy storage and conversion, *Nanoscale* 7 (2015) 17590–17610.

[17] A. Thomas, C. Janáky, G.F. Samu, M.N. Huda, P. Sarker, J.P. Liu, V. van Nguyen, E.H. Wang, K.A. Schug, K. Rajeshwar, Time- and energy-efficient solution combustion synthesis of binary metal tungstate nanoparticles with enhanced photocatalytic activity, *ChemSusChem* 8 (2015) 1652–1663.

[18] A. Kormányos, A. Thomas, M.N. Huda, P. Sarker, J.P. Liu, N. Poudyal, C. Janáky, K. Rajeshwar, Solution combustion synthesis, characterization, and photoelectrochemistry of $CuNb_2O_6$ and $ZnNb_2O_6$ nanoparticles, *J. Phys. Chem. C* 120 (2016) 16024–16034.

[19] V. Etacheri, C. Di Valentini, J. Schneider, D. Bahnemann, S.C. Pillai, Visible-light activation of TiO_2 photocatalysts: advances in theory and experiments, *J. Photochem. Photobiol. C: Photochem. Rev.* 25 (2015) 1–29.

[20] B.D. Alexander, P.J. Kulesza, I. Rutkowska, R. Solarska, J. Augustynski, Metal oxide photoanodes for solar hydrogen production, *J. Mater. Chem.* 18 (2008) 2298–2303.

[21] C. Janáky, D. Hursán, B. Endrődi, W. Chanmanee, D. Roy, D. Liu, N.R. de Tacconi, B.H. Dennis, K. Rajeshwar, Electro- and photoreduction of carbon dioxide: the twain shall meet at copper oxide/copper interfaces, *ACS Energy Lett.* 1 (2016) 332–338.

[22] A. Kudo, S. Hijii, H_2 or O_2 evolution from aqueous solutions on layered oxide photocatalysts consisting of Bi^{3+} with $6s^2$ configuration and d^0 transition metal ions, *Chem. Lett.* 28 (1999) 1103–1104.

[23] C. Janáky, K. Rajeshwar, N.R. de Tacconi, W. Chanmanee, M.N. Huda, Tungsten-based oxide semiconductors for solar hydrogen generation, *Catal. Today* 199 (2013) 53–64.

[24] W. Wei, Y. Dai, B. Huang, First-principles characterization of Bi -based photocatalysts: $Bi_{12}TiO_{20}$, $Bi_2Ti_2O_7$, and $Bi_4Ti_3O_{12}$, *J. Phys. Chem. C* 113 (2009) 5658–5663.

[25] T. Kidchob, L. Malfatti, D. Marongiu, S. Enzo, P. Innocenzi, Sol-gel processing of $Bi_2Ti_2O_7$ and $Bi_2Ti_4O_{11}$ films with photocatalytic activity, *J. Am. Ceram. Soc.* 93 (2010) 2897–2902.

[26] J.R. Esquivel-Elizondo, B.B. Hinojosa, J.C. Nino, $Bi_2Ti_2O_7$: it is not what you have read, *Chem. Mater.* 23 (2011) 4965–4974.

[27] A. McInnes, J.S. Sagu, K.G.U. Wijayanthan, Fabrication and photoelectrochemical studies of $Bi_2Ti_2O_7$ pyrochlore thin films by aerosol assisted chemical vapour deposition, *Mater. Lett.* 137 (2014) 214–217.

[28] Z. Bian, Y. Huo, Y. Zhang, J. Zhu, Y. Lu, H. Li, Aerosol-spay assisted assembly of $Bi_2Ti_2O_7$ crystals in uniform porous microspheres with enhanced photocatalytic activity, *Appl. Catal. B: Environ.* 91 (2009) 247–253.

[29] A.L. Hector, S.B. Wiggins, Synthesis and structural study of stoichiometric $Bi_2Ti_2O_7$ pyrochlore, *J. Solid State Chem.* 177 (2004) 139–145.

[30] I. Radosavljevic, J.S.O. Evans, A.W. Sleight, Synthesis and structure of pyrochlore-type bismuth titanate, *J. Solid State Chem.* 136 (1998) 63–66.

[31] S. Murugesan, V. Subramanian, Robust synthesis of bismuth titanate pyrochlore nanorods and their photocatalytic applications, *Chem. Commun.* 14 (2009) 5109–5111.

[32] J. Hou, S. Jiao, H. Zhu, R.V. Kumar, Bismuth titanate pyrochlore microspheres: directed synthesis and their visible light photocatalytic activity, *J. Solid State Chem.* 184 (2011) 154–158.

[33] J. Ren, G. Liu, Y. Wang, Q. Shi, A novel method for the preparation of $Bi_2Ti_2O_7$ pyrochlore, *Mater. Lett.* 76 (2012) 184–186.

[34] O. Merka, D.W. Bahnemann, M. Wark, Photocatalytic hydrogen production with non-stoichiometric pyrochlore bismuth titanate, *Catal. Today* 225 (2014) 102–110.

[35] F.E. Oropeza, I.J. Villar-Garcia, R.G. Palgrave, D.J. Payne, A solution chemistry approach to epitaxial growth and stabilisation of $Bi_2Ti_2O_7$ films, *J. Mater. Chem. A* 2 (2014) 18241–18245.

[36] R.J. Walker, A. Pougin, F.E. Oropeza, I.J. Villar-Garcia, M.P. Ryan, J. Strunk, D.J. Payne, Surface termination and CO_2 adsorption onto bismuth pyrochlore oxides, *Chem. Mater.* 28 (2016) 90–96.

[37] I.V. Piir, M.S. Koroleva, Y.I. Ryabkov, D.A. Korolev, N.V. Chezhina, V.G. Semenov, V.V. Panchuk, Bismuth iron titanate pyrochlores: thermostability, structure and properties, *J. Solid State Chem.* 204 (2013) 245–250.

[38] S. Gupta, V. Subramanian, Encapsulating $Bi_2Ti_2O_7$ (BTO) with reduced graphene oxide (RGO): An effective strategy to enhance photocatalytic and photoelectrocatalytic activity of BTO, *ACS Appl. Mater. Interfaces* 6 (2014) 18597–18608.

[39] J. Selvaraj, S. Gupta, R. Anand, S. Fiechter, V. Subramanian, How beneficial is reduced graphene oxide (RGO) for long-term photo generated charge transport in bismuth titanate–RGO nanocomposite films? *J. Electrochem. Soc.* 163 (2016) H147–H153.

[40] J. Yi, X. Yuan, H. Wang, H. Yu, F. Peng, Preparation of $Bi_2Ti_2O_7/TiO_2$ nanocomposites and their photocatalytic performance under visible light irradiation, *Mater. Des.* 86 (2015) 152–155.

[41] H. Shi, H. Tan, W. Zhu, Z. Sun, Y. Ma, E. Wang, Electrospun Cr-doped $Bi_4Ti_3O_{12}/Bi_2Ti_2O_7$ heterostructure fibers with enhanced visible-light photocatalytic properties, *J. Mater. Chem. A* 3 (2015) 6586–6591.

[42] C.L. Mayfield, M.N. Huda, Free energy landscape approach to aid pure phase synthesis of transition metal ($X = Cr, Mn$ and Fe) doped bismuth titanate ($Bi_2Ti_2O_7$), *J. Cryst. Growth* 444 (2016) 46–54.

[43] C.L. Mayfield, V. Subramanian, M.N. Huda, Free energy dependence of pure phase iron doped bismuth titanate from first principles calculations, *J. Phys.: Condens. Matter* 27 (2015) 315502–315512.

[44] S. Murugesan, M.N. Huda, Y. Yan, M.M. Al-Jassim, V. Subramanian, Band-engineered bismuth titanate pyrochlores for visible light photocatalysis, *J. Phys. Chem. C* 114 (2010) 10598–10605.

[45] W. Ragsdale, S. Gupta, K. Conard, S. Delacruz, V. Subramanian, Photocatalytic activity of Fe-modified bismuth titanate pyrochlores: insights into its stability, photoelectrochemical, and optical responses, *Appl. Catal. B Environ.* 180 (2016) 442–450.

[46] B. Allured, S. DelaCruz, T. Darling, M.N. Huda, V. Subramanian, Enhancing the visible light absorbance of $Bi_2Ti_2O_7$ through Fe-substitution and its effects on photocatalytic hydrogen evolution, *Appl. Catal. B: Environ.* 144 (2014) 261–268.

[47] S. Gupta, L. De Leon, V. Subramanian, Mn-modified $Bi_2Ti_2O_7$ photocatalysts: bandgap engineered multifunctional photocatalysts for hydrogen generation, *Phys. Chem. Chem. Phys.* 16 (2014) 12719–12727.

[48] S. Naz, S.K. Durrani, A.H. Qureshi, M.A. Hussain, N. Hussain, Nanosized bismuth titanate ($Bi_4Ti_3O_{12}$) system drive through auto-combustion process by using suspension titania (TiO_2), *J. Therm. Anal. Calorim.* 114 (2013) 719–723.

[49] Z.S. Macedo, C.R. Ferrari, A.C. Hernandes, Self-propagation high-temperature synthesis of bismuth titanate, *Powder Technol.* 139 (2004) 175–179.

[50] K.C. Patil, M.S. Hegde, T. Rattan, S.T. Aruna, *Chemistry of Nanocrystalline Oxide Materials – Combustion Synthesis, Properties and Applications*, World Scientific Publishing Co. Ltd. Pte., 2008.

[51] A.C. Larson, R.B. Von Dreele, General structure analysis system (GSAS), *Los Alamos Natl. Lab. Rep.* (2004) 86–748.

[52] B.H. Toby, EXPGUI, a graphical user interface for GSAS, *J. Appl. Crystallogr.* 34 (2001) 210–213.

[53] H.M. Rietveld, A profile refinement method for nuclear and magnetic structures, *J. Appl. Crystallogr.* 2 (1969) 65–71.

[54] R.D. Shannon, Revised effective ionic radii and systematic studies of interatomic distances in halides and chalcogenides, *Acta Crystallogr. Sect. A* 32 (1976) 751–767.

[55] N.S. McIntyre, D.G. Zetaruk, X-ray photoelectron spectroscopic studies of iron oxides, *Anal. Chem.* 49 (1977) 1521–1529.

[56] A.P. Grosvenor, B.A. Kobe, M.C. Biesinger, N.S. McIntyre, Investigation of multiplet splitting of $Fe\ 2p$ XPS spectra and bonding in iron compounds, *Surf. Interface Anal.* 36 (2004) 1564–1574.

[57] L. Kang, H. An, T.H. Kim, D.-H. Lee, K.-S. Park, B. Swain, C.G. Lee, S. Nahm, Effect of controlled Mn doping on transition of oxygen vacancies in $Bi_2Ti_2O_7$ thin films: an electrochemical study, *Appl. Surf. Sci.* (2017), <http://dx.doi.org/10.1016/j.apsusc.2016.12.162> (in press).

[58] K.-H. Cho, M.-G. Kang, H.W. Jang, H.Y. Shin, C.-Y. Kang, S.-J. Yoon, Significantly reduced leakage currents in organic thin film transistors with Mn-doped $Bi_2Ti_2O_7$ high- κ gate dielectrics, *Phys. Status Solidi – Rapid Res. Lett.* 6 (2012) 208–210.

[59] R. Beranek, (Photo)electrochemical methods for the determination of the band edge positions of TiO_2 -based nanomaterials, *Adv. Phys. Chem.* 2011 (2011) 1–20.

[60] K. Rajeshwar, Fundamentals of semiconductor electrochemistry and photoelectrochemistry, in: A.J. Bard, M. Stratmann, S. Licht (Eds.), *Encyclopedia of Electrochemistry, Volume 6 Semiconductor Electrodes and Photoelectrochemistry*, 1st ed., Wiley-VCH Verlag, 2002, pp. 1–53.

[61] H. Liu, Y. Chen, G. Tian, Z. Ren, C. Tian, H. Fu, Visible-light-induced self-cleaning property of $\text{Bi}_2\text{Ti}_2\text{O}_7\text{--TiO}_2$ composite nanowire arrays, *Langmuir* 31 (2015) 5962–5969.

[62] G.F. Samu, Á. Veres, S.P. Tallósy, L. Janovák, I. Dékány, A. Yepez, R. Luque, C. Janáky, Photocatalytic, photoelectrochemical, and antibacterial activity of benign-by-design mechanochemically synthesized metal oxide nanomaterials, *Catal. Today* 284 (2017) 3–10, <http://dx.doi.org/10.1016/j.cattod.2016.07.010>.

[63] M.C. Biesinger, B.P. Payne, A.P. Grosvenor, L.W.M. Lau, A.R. Gerson, R.S.C. Smart, Resolving surface chemical states in XPS analysis of first row transition metals, oxides and hydroxides: Cr, Mn, Fe, Co and Ni, *Appl. Surf. Sci.* 257 (2011) 2717–2730.

[64] S. Xie, P. Huang, J.J. Kružic, X. Zeng, H. Qian, A highly efficient degradation mechanism of methyl orange using Fe-based metallic glass powders, *Sci. Rep.* 6 (2016) 21947–21956.